

## ARTICLE

Received 10 Jun 2010 | Accepted 17 Mar 2011 | Published 12 Apr 2011

DOI: 10.1038/ncomms1280

# Molecular dynamics of single-particle impacts predicts phase diagrams for large scale pattern formation

Scott A. Norris<sup>1,3</sup>, Juha Samela<sup>2</sup>, Laura Bukonte<sup>2</sup>, Marie Backman<sup>2</sup>, Flyura Djurabekova<sup>2</sup>, Kai Nordlund<sup>2</sup>, Charbel S. Madi<sup>3</sup>, Michael P. Brenner<sup>3</sup> & Michael J. Aziz<sup>3</sup>

Energetic particle irradiation can cause surface ultra-smoothing, self-organized nanoscale pattern formation or degradation of the structural integrity of nuclear reactor components. A fundamental understanding of the mechanisms governing the selection among these outcomes has been elusive. Here we predict the mechanism governing the transition from pattern formation to flatness using only parameter-free molecular dynamics simulations of single-ion impacts as input into a multiscale analysis, obtaining good agreement with experiment. Our results overturn the paradigm attributing these phenomena to the removal of target atoms via sputter erosion: the mechanism dominating both stability and instability is the impact-induced redistribution of target atoms that are not sputtered away, with erosive effects being essentially irrelevant. We discuss the potential implications for the formation of a mysterious nanoscale topography, leading to surface degradation, of tungsten plasma-facing fusion reactor walls. Consideration of impact-induced redistribution processes may lead to a new design criterion for stability under irradiation.

<sup>1</sup> Department of Mathematics, Southern Methodist University, Dallas, Texas 75205, USA. <sup>2</sup> Department of Physics and Helsinki Institute of Physics, FIN-0014 University of Helsinki, PO Box 43, Helsinki, Finland. <sup>3</sup> Harvard School of Engineering and Applied Sciences, Cambridge, Massachusetts 02138, USA. Correspondence and requests for materials should be addressed to S.A.N. (email: snorris@smu.edu) or to M.J.A. (email: maziz@harvard.edu).

Solids irradiated by energetic beams can, depending on environmental parameters, undergo either surface ultra-smoothing<sup>1</sup> or self-organized nanoscale pattern formation<sup>2</sup>; the desirability of the latter outcome depends on the context. On the one hand, observations of periodic patterns including high-aspect ratio quantum dots<sup>3</sup>, with occasional long-range order<sup>4</sup> and characteristic spacing, as small as 7 nm (ref. 5), have stimulated interest in self-organized pattern formation as a means of sub-lithographic nanofabrication<sup>6</sup>. On the other hand, extended exposure to energetic particle irradiation can lead to the structural degradation of fission and fusion reactor components<sup>7,8</sup>. Hence, it is important to be able to predict the expected behaviour within a given environment. Unfortunately, precisely which physical effects cause observed transitions between different regimes<sup>9,10</sup> has remained a matter of speculation<sup>11</sup>.

At particle energies between  $10^2$  and  $10^4$  eV, the irradiation process is dominated by the nuclear collision cascade caused by impact<sup>12,13</sup>. Displaced atoms that reach the surface with enough kinetic energy to leave are permanently sputtered away; all other displaced atoms come to rest within the solid or on the surface after phonon emission times of  $\sim 10^{-12}$  s. These processes contribute prompt erosive<sup>14,15</sup> and prompt redistributive<sup>11,16,17</sup> components of morphology evolution and are collectively denoted  $P[\mathbf{x}]$ .

For most materials other than elemental metals, the damage resulting from accumulated impacts quickly ( $\sim 10^{-3}$  s) leads to the amorphization of a thin layer of target material. Over much longer time scales ( $\sim 100$  s), mass transport within this layer by kinetic relaxation processes causes a gradual relaxational effect<sup>14,18</sup>. Hence, to the prompt term  $P[\mathbf{x}]$  we add a phenomenological term for the gradual relaxation regime denoted  $G[\mathbf{x}]$ , assuming a mechanism of ion-enhanced viscous flow, which is expected to predominate in irradiated amorphous materials near room temperature<sup>18</sup>. The prompt and gradual contributions to the rate of motion of the surface in the normal direction  $v_n$  then superpose:

$$v_n = P[\mathbf{x}] + G[\mathbf{x}]. \quad (1)$$

The prompt regime may be characterized using molecular dynamics (MD) simulations<sup>17,19</sup> or experimental methods<sup>20</sup>. Given data from many impact events, we may obtain the ‘crater function’  $\Delta h(x-x', \theta)$  describing the average change in local surface height at a point  $x$  resulting from a single-ion impact at  $x'$ , with incidence angle  $\theta$  (a potential dependence on the surface shape, which is very difficult to capture with MD, is left for future work). We then upscale the crater function into a continuum partial differential equation (PDE) for the surface evolution using a multiscale framework. The theoretical formalism for this process is described in more detail in the Supplementary Information and in ref. 21; here we provide a brief summary of the important points for the linear case.

Given the crater function  $\Delta h$  and the flux distribution  $I(\mathbf{x})$ , we write the prompt contribution to surface evolution as a flux-weighted integral of the crater function<sup>11,22</sup>:

$$P[\mathbf{x}] = \int I(\mathbf{x}') \Delta h(\mathbf{x} - \mathbf{x}', \theta) d\mathbf{x}' \quad (2)$$

A well-known observation in the field is that scale of the craters is much smaller than the scale of the resulting pattern and of the flux distribution. To exploit this fact, we use a formal multiple-scale analysis, based on a small parameter  $\varepsilon$  related to the ratio of impact scale to pattern scale. This formalism allows ready separation of the spatial dependence of the crater shape (fast) from that of the pattern (slow), and leads eventually to an upscaled description of the prompt regime in moment form:

$$P[\mathbf{x}] = (IM^{(0)}) + \varepsilon \nabla_{\mathbf{S}} \cdot (IM^{(1)}) + \frac{1}{2} \varepsilon^2 \nabla_{\mathbf{S}} \cdot \nabla_{\mathbf{S}} \cdot (IM^{(2)}) + \dots \quad (3)$$

Here the  $\nabla_{\mathbf{S}}$  represent surface divergences, and the (increasing-order) tensors  $M^{(i)}$  are simply the angle-dependent moments of the crater function  $\Delta h$ .

Pattern-forming predictions are obtained by linearizing equation (1), and examining the stability of the linearization as a function of the laboratory incidence angle  $\theta$ . The linearization process follows that given in ref. 14, and in an appropriate frame of reference one finds that the magnitude of infinitesimal perturbations  $h$  away from a flat surface evolve, to leading order in  $\varepsilon$ , according to the PDE

$$\frac{\partial h(x, y, t)}{\partial t} = \left( S_X(\theta) \frac{\partial^2 h}{\partial x^2} + S_Y(\theta) \frac{\partial^2 h}{\partial y^2} \right) - B \nabla^4 h, \quad (4)$$

where the angle-dependent coefficients

$$S_X(\theta) = I_0 \frac{d}{d\theta} [M^{(1)}(\theta) \cos(\theta)] \quad (5)$$

$$S_Y(\theta) = I_0 M^{(1)}(\theta) \cos(\theta) \cot(\theta)$$

are determined from the first moments obtained using MD, and the constant coefficient  $B$  is estimated from independent experiments. The structure of equation (4) indicates that linear stability is determined strictly by the signs of the calculated coefficients ( $S_X, S_Y$ ): for values of  $\theta$  where either of these coefficients is negative, linearly unstable modes exist and we expect patterns, whereas for values of  $\theta$  where they are both positive we expect flat, stable surfaces.

## Results

**Phase diagram prediction.** To turn equation (4) into a prediction, it is necessary to obtain the angle-dependent moment  $M^{(1)}$ . Using MD simulations of single impacts, we collected angle-dependent moments for Si irradiated by  $\text{Ar}^+$  ions at both 100 and 250 eV (the zeroth moment  $M^{(0)}$ , which is proportional to the number of atoms sputtered per ion, was also obtained). For each energy, 200 ion impacts were simulated at incidence angles in  $5^\circ$  increments between  $0^\circ$  and  $90^\circ$ , yielding average moments as summarized in Figure 1. For use within our analytical framework, we fit these moments to Fourier series constrained by symmetry conditions and by the observation that all moments tend to zero at  $\theta = \pm 90^\circ$ . Finally, the moments were separated into redistributive and erosive components: contributions from displaced atoms coming to rest within or on the solid, and contributions from atoms permanently sputtered away, respectively. For both energies, the redistributive first moments are much larger in magnitude than—and have the opposite sign of—their erosive counterparts. The implication, and main finding of this work, is that redistributive effects completely dominate erosive effects, except possibly at the highest (grazing) angles where all moments tend to zero.

**Comparison with experiment.** To corroborate this finding, we calculate in Figure 2 the coefficients (5) of the linearized equation (4) for the 250 eV moments, and compare the pattern wavelengths they predict to experimental observations in the same environmental conditions<sup>23</sup>. (Note: Clean linear experimental data at 100 eV are not currently available. Also, the ripples originally reported in ref. 23 at 250 eV for angles below  $20^\circ$  have been omitted because those authors have recently shown them to be an experimental artefact.) The agreement is excellent, with two minor exceptions. First, the small quantitative difference between predicted and observed phase boundaries—which depends only on the shape of  $S_X(\theta)$ —could readily arise from the approximate nature of the classical potential, on which our simulations are based (unlike the phase boundary, precise wavelength values depend on the value of  $B$ , which could only be estimated). Second, the measured moments do not predict a transition to perpendicular modes at the highest angles; this could be due to our neglect of explicit curvature dependence in the

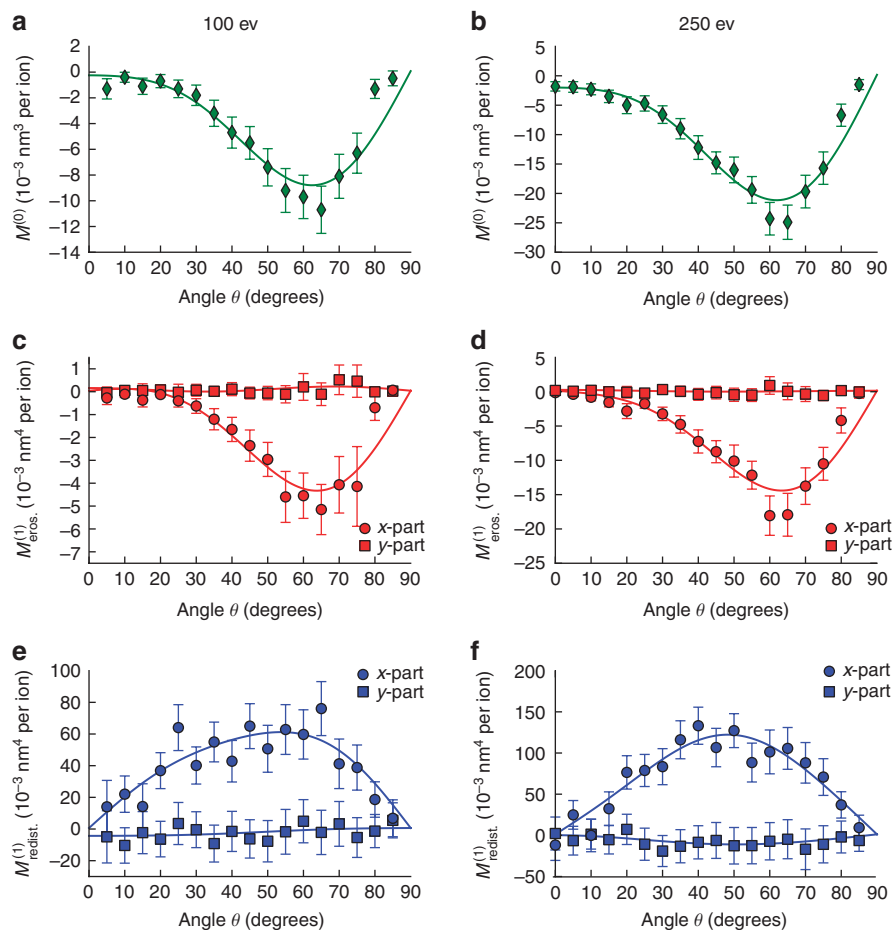


**Figure 1 | Moments obtained from molecular dynamics.** Fitted average angle-dependent moments of the crater function  $\Delta h(x,y)$  as determined from molecular dynamics, for both 100 eV (left column) and 250 eV (right column). Error bars indicate a standard 95% confidence interval ( $\pm 1.96$  s.d.) associated with the 200 simulations at each angle. **(a, b)** Zeroth erosive moment  $M^{(0)}$  (sputter yield times atomic volume). **(c, d)** First erosive moments  $M_{\text{erosive}}^{(1)}$ . **(e, f)** First redistributive moments  $M_{\text{redist.}}^{(1)}$ . Each of the first moments contains components in both the downbeam or 'x'-direction (circles), and also the crossbeam or 'y'-direction (squares), with the crossbeam components expected to be zero from symmetry arguments<sup>21</sup>. At both energies, redistribution strongly dominates erosion.

crater function, but additional physical effects such as shadowing and surface channeling—not addressed here—are known to be important at grazing angles. Despite these limitations of our approach, when one considers the lack of any free parameters in the theory, the agreement with experiment is remarkably good. The agreement remains good even when the erosive coefficients are omitted, and the similar shapes of the redistributive moments at 100 and 250 eV is consistent with the reported<sup>23</sup> energy insensitivity of the stability/instability phase boundary.

## Discussion

Existing uses of MD crater data for investigations of surface pattern-forming are entirely numerical in nature<sup>24</sup>, and could be viewed as a scheme for numerically integrating equation (2). In contrast, our analytical upscaling of equation (2) into the moment form (3) is notable for several reasons. First, it illustrates exactly which qualities of the crater—namely, its moments—have the dominant role in surface evolution. Second, the moment form can be linearized, allowing predictions of stability boundaries, and changes to those boundaries as crater shape is varied. Third, moments are readily obtainable directly by MD simulation, and converge with far fewer trials than do descriptions of the entire crater function used in previous works. Last, although atomistic methods have been used in the past to obtain the amplitude of a single term in a PDE obtained

by phenomenological modelling<sup>17,25–27</sup>, we believe this is the first derivation of an entire PDE from MD results.

A crucial component of our approach is that the crater function  $\Delta h$ —and hence the moments  $M^{(i)}$ —contains the contributions of both erosion and mass redistribution. Whereas these effects have traditionally been treated separately by unrelated phenomenological models, viewing the crater function as fundamental integrates erosion and redistribution into a unified description, allowing both processes to be treated identically and readily separated and compared. Indeed, this approach has permitted us to confirm for the first time conjectures<sup>11,19,22</sup> that the stability of irradiated surfaces could be dominated by redistributive effects. The most striking aspect of this result is the logical conclusion that erosion is essentially irrelevant for determining the patterns: according to Figure 2 the contributions of redistribution to the  $S$  coefficients, which determine stability and patterns, are about an order of magnitude greater and opposite in sign. This conclusion overturns the erosion-based paradigm that has dominated the field for two decades<sup>14</sup> and we suggest its replacement with a redistribution-based paradigm.

An important direction for future research is identifying the range of irradiation energies over which our conclusion holds. Because the scale of the impact increases with the energy, higher energies require larger simulation targets, increasing the computational cost of MD simulations. However, preliminary investigations

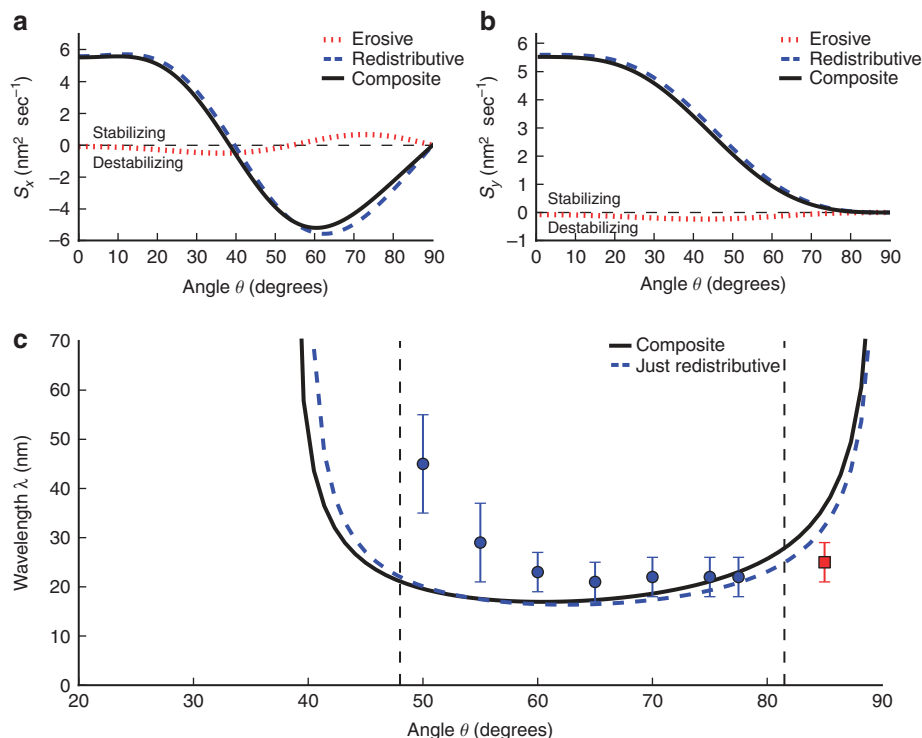


**Figure 2 | Predictions and comparison with experiment.** Comparison between predicted and measured wavelength for Si irradiated by Ar<sup>+</sup> at 250 eV. Coefficients  $S_x(\theta)$  and  $S_y(\theta)$  in the linearized evolution equation (4) were calculated with a flux of  $f = 3.5 \times 10^{15}$  ions cm<sup>-2</sup> s<sup>-1</sup> for comparison with experimental conditions<sup>23</sup>. **(a, b)** Coefficients of  $\partial^2 h / \partial x^2$  and  $\partial^2 h / \partial y^2$  in the linearized evolution equation using the experimental flux. These coefficients are dominated by redistributive effects. **(c)** Comparison of predicted ripple wavelengths with average experimentally observed wavelengths (see ref. 23). Circles/squares indicate experimental patterns with wavevector parallel/perpendicular to the beam (parallel mode and perpendicular mode, respectively), and the vertical dashed black lines indicate experimental phase boundaries. Error bars indicate the full-width at half-maximum measure of the peaks in the power spectral density associated with atomic force microscopy images of experimental samples. On top of this, the solid black line indicates our predicted wavelengths (which are all parallel mode), and the dashed blue line indicates the wavelengths predicted if erosion were neglected entirely.

of silicon irradiated by argon at 1 keV, at selected angles spanning the experimental transition point, are so far consistent with our conclusions, and experimental results at 1 keV lead to the same conclusion<sup>28</sup>. As this energy is typical of pattern-forming investigations within the literature, we conclude that it remains to be determined whether erosion is actually important for stability or pattern formation in any physical experiment to date.

We believe the phenomena reported in this paper are applicable to a wide variety of systems. For instance, our predictions may be relevant in the context of tungsten plasma-facing fusion reactor walls, in which low-sputter yield (atoms removed per incident particle) has been an important design criterion in the selection of tungsten for surfaces that must be exposed to large plasma particle fluxes for extended periods. Because the average helium ion energy is only  $\sim 60$  eV and the threshold energy for sputter removal of tungsten is  $\sim 100$  eV, this material has been considered impervious to the effects of erosion. However, despite a sputter erosion rate that is essentially zero, plasma-facing tungsten, nevertheless, develops under some conditions a nanoscale topography leading to surface degradation<sup>8</sup>—an outcome that appears mysterious within the erosion-based paradigm. The crater function-based analysis presented here suggests that such degradation may originate in impact-induced target atom redistribution effects. A re-analysis of the simulations performed in ref. 29 on helium-irradiated tungsten shows that, after 4,000 consecutive impacts at 100 eV from an incidence angle of 25°, a cumulative displacement field emerges with a clear downbeam bias (Fig. 3). This suggests a redistributive moment that may produce the same stability properties as for those measured

above. If this conjecture turns out to be correct, then an extremely low-sputter erosion rate would be an insufficient design criterion for morphologically stable solid surfaces under energetic particle irradiation, and ultimately crater function engineering considerations may provide a more refined materials design criterion.

## Methods

**Simulation environment.** Our MD simulation environment consists of an amorphous,  $20 \times 20 \times 10$  nm<sup>3</sup> Si target consisting of 219,488 atoms, with slab boundary conditions (free boundary in the incoming ion direction, and periodic boundaries in the other two lateral directions)<sup>30</sup>. The target itself was created using the Wooten/Winer/Weaire method<sup>31</sup>. Because this method is computationally expensive for large targets, we first constructed a smaller  $10 \times 10 \times 10$  nm<sup>3</sup> block, and then copied it four times to achieve the desired size. The resulting composite was then annealed with the environment-dependent interatomic potential<sup>32</sup>. This gives an optimized amorphous structure with realistic density, and in which most of the Si atoms have coordination number 4.

The target was then bombarded with Ar<sup>+</sup> at 100 and 250 eV at different incidence angles, with random impact points and azimuthal angles, at an ambient temperature of 0 K. During bombardment, the interaction between Si atoms was again described using the environment-dependent interatomic potential, which gives a good agreement between simulated and experimental sputtering yields<sup>33</sup>, whereas the Ar–Si interaction was a potential calculated for the Ar–Si dimer<sup>34</sup>. Kinetic energy was gradually removed during the simulations from 1 nm borders of the cell to prevent it from re-entering the impact area via the periodic boundary conditions used in the simulations.

The simulation arrangements and their suitability for cluster and ion bombardment simulations are discussed in more detail in refs 33, 35–37.

**Obtaining moments.** For each impact, simulations totalling 15 ps were run, which was enough time for atomic motion to settle to the level of thermal vibration. Final atomic positions were then obtained by averaging the atomic positions for a further

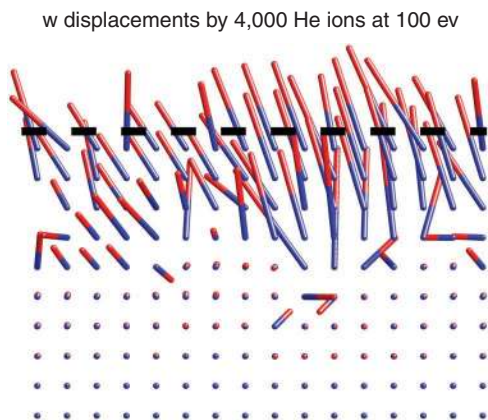


**Figure 3 | Downbeam displacements in helium-irradiated tungsten.**

Inside a fusion reactor, He irradiates the W walls at low energies (of order 100 eV), generating essentially zero sputter erosion and very little displacement, complicating the isolation within an MD simulation of a clear average signal. However, the cumulative displacement field after 4,000 consecutive off-normal impacts at 100 eV shows a clear downbeam bias. Here impinging helium ions come from the upper right, at an angle of 25° from normal. The sticks combine the initial and final position of atoms that were initially in a half a unit cell thick cross-section through the simulation cell. The blue ends of the sticks indicate the initial positions and the red ends the final positions of the atoms. The surface is located at the top (from a re-analysis of data in ref. 29).

5 ps. Before analysis, this set of post-impact atomic positions was adjusted in two important ways. First, the global average displacement of each atom over all impacts at a given incidence angle was subtracted from its post-impact position for each impact at that angle, to remove target-specific effects from our measurements (see Supplementary Fig. S1). Second, an observed shear of the entire target in the downbeam direction—caused by the finite target size—was fitted from data near the bottom of the target, and also subtracted from the post-impact positions (see Supplementary Fig. S2).

From the initial and adjusted final atomic positions, moments were obtained by assuming that densities in the amorphous layer must attain a steady state over time<sup>21</sup>. Consequently, we project defect distributions immediately to the target surface for the purpose of quantifying crater functions. Within this scheme, the effects of erosion and redistribution are readily separated. Erosive moments are obtained by assigning a height loss at each location proportional to the number of sputtered atoms originating from that location. Similarly, redistributive moments were obtained by assigning height losses at initial atomic positions and height gains at final atomic positions. This strategy produced the data points in Figure 1; the data were then fitted to simple three-term Fourier series to generate the curves in the same figure.

Additional details of our simulation environment are available in the Supplementary Information.

## References

1. Yamada, I., Matsuo, J., Toyoda, N. & Kirkpatrick, A. Materials processing by gas cluster ion beams. *Mat. Sci. Eng. R* **34**, 231–295 (2001).
2. Chan, W. L. & Chason, E. Making waves: kinetic processes controlling surface evolution during low energy ion sputtering. *J. Appl. Phys.* **101**, 121301 (2007).
3. Fackso, S. *et al.* Formation of ordered nanoscale semiconductor dots by ion sputtering. *Science* **285**, 1551–1553 (1999).
4. Ziberi, B., Frost, F., Höche, T. & Rauschenbach, B. Ripple pattern formation on silicon surfaces by low-energy ion-beam erosion: experiment and theory. *Phys. Rev. B* **72**, 235310 (2005).
5. Wei, Q. *et al.* Ordered nanocrystals on argon ion sputtered polymer film. *Chem. Phys. Lett.* **452**, 124–128 (2008).
6. Cuenat, A. *et al.* Lateral templating for guided self-organization of sputter morphologies. *Adv. Mater.* **17**, 2845–2849 (2005).
7. Singh, B. N. & Zinkle, S. J. Defect accumulation in pure fcc metals in the transient regime: a review. *J. Nucl. Mater.* **206**, 212–229 (1993).
8. Baldwin, M. J. & Doerner, R. P. Helium induced nanoscopic morphology on tungsten under fusion relevant plasma conditions. *Nucl. Fusion* **48**, 035001 (2008).
9. Ziberi, B., Frost, F., Tartz, M., Neumann, H. & Rauschenbach, B. Ripple rotation, pattern transitions, and long range ordered dots on silicon by ion beam erosion. *Appl. Phys. Lett.* **92**, 063102 (2008).

10. Madi, C. S. *et al.* Multiple bifurcation types and the linear dynamics of ion sputtered surfaces. *Phys. Rev. Lett.* **101**, 246102 (2008).
11. Davidovitch, B. P., Aziz, M. J. & Brenner, M. P. On the stabilization of ion sputtered surfaces. *Phys. Rev. B* **76**, 205420 (2007).
12. Sigmund, P. Theory of sputtering. I. Sputtering yield of amorphous and polycrystalline targets. *Phys. Rev.* **184**, 383–416 (1969).
13. Sigmund, P. A mechanism of surface micro-roughening by ion bombardment. *J. Mater. Sci.* **8**, c1545–c1553 (1973).
14. Bradley, R. M. & Harper, J. M. Theory of ripple topography induced by ion bombardment. *J. Vac. Sci. Technol.* **6**, 2390–2395 (1988).
15. Makeev, M. A., Cuerno, R. & Barabási, A.-L. Morphology of ion-sputtered surfaces. *Nucl. Instrum. Methods Phys. Res. B* **197**, 185–227 (2002).
16. Carter, G. & Vishnyakov, V. Roughening and ripple instabilities on ion-bombarded Si. *Phys. Rev. B* **54**, 17647–17653 (1996).
17. Moseler, M., Gumbsch, P., Casiraghi, C., Ferrari, A. C. & Robertson, J. The ultrasmoothness of diamond-like carbon surfaces. *Science* **309**, 1545–1548 (2005).
18. Umbach, C. C., Headrick, R. L. & Chang, K.-C. Spontaneous nanoscale corrugation of ion-eroded SiO<sub>2</sub>: the role of ion-irradiation-enhanced viscous flow. *Phys. Rev. Lett.* **87**, 246104 (2001).
19. Kalyanasundaram, N., Ghazisaeidi, M., Freund, J. B. & Johnson, H. T. Single impact crater functions for ion bombardment of silicon. *Appl. Phys. Lett.* **92**, 131909 (2008).
20. Costantini, G., de Mongeot, F. B., Boragno, C. & Valbusa, U. Is ion sputtering always a “negative homoepitaxial deposition”? *Phys. Rev. Lett.* **86**, 838–841 (2001).
21. Norris, S. A., Brenner, M. P. & Aziz, M. J. From crater functions to partial differential equations: a new approach to ion bombardment induced nonequilibrium pattern formation. *J. Phys. Condens. Matt.* **21**, 224017 (2009).
22. Aziz, M. J. Nanoscale morphology control using ion beams. *Matematisk-fysiske Meddelelser* **52**, 187–206 (2006).
23. Madi, C. S., George, H. B. & Aziz, M. J. Linear stability and instability patterns in ion-sputtered silicon. *J. Phys. Condens. Matt.* **21**, 224010 (2009).
24. Kalyanasundaram, N., Freund, J. B. & Johnson, H. T. A multiscale crater function model for ion-induced pattern formation in silicon. *J. Phys. Condens. Matt.* **21**, 224018 (2009).
25. Enrique, R. A. & Bellon, P. Compositional patterning in systems driven by competing dynamics of different length scale. *Phys. Rev. Lett.* **84**, 2885–2888 (2000).
26. Zhou, H., Zhou, L., Özyaydin, G., Ludwig, K. F. Jr & Headrick, R. L. Mechanisms of pattern formation and smoothing induced by ion-beam erosion. *Phys. Rev. B* **78**, 165404 (2008).
27. Headrick, R. L. & Zhou, H. Ripple formation and smoothing on insulating surfaces. *J. Phys. Condens. Matt.* **21**, 224005 (2009).
28. Madi, C. S., Anzenberg, E., Ludwig Jr., K. F. & Aziz, M. J. Mass redistribution causes the structural richness of ion-irradiated surfaces. *Phys. Rev. Lett.* **106**, 066101 (2011).
29. Henriksson, K., Nordlund, K. & Keinonen, J. Molecular dynamics simulations of helium cluster formation in tungsten. *Nucl. Instrum. Methods Phys. Res. B* **244**, 377–391 (2006).
30. Samela, J., Norris, S. A., Nordlund, K. & Aziz, M. J. Optimization of large amorphous silicon and silica structures for molecular dynamics simulations of energetic impacts. *Nucl. Instrum. Methods Phys. Res. B* (doi.org/10.1016/j.nimb.2010.11.017) (2011).
31. Wooten, F., Winer, K. & Weaire, D. Computer generation of structural models of amorphous Si and Ge. *Phys. Rev. Lett.* **54**, 1392–1395 (1985).
32. Bazant, M. Z., Kaxiras, E. & Justo, J. F. Environment-dependent interatomic potential for bulk silicon. *Phys. Rev. B* **56**, 8542–8552 (1997).
33. Samela, J., Nordlund, K., Keinonen, J. & Popok, V. N. Comparison of silicon potentials for cluster bombardment simulations. *Nucl. Instrum. Methods Phys. Res. B* **255**, 253–258 (2007).
34. Nordlund, K., Runeberg, N. & Sundholm, D. Repulsive interatomic potentials calculated using hartree-fock and density-functional theory methods. *Nucl. Instrum. Methods Phys. Res. B* **132**, 1–8 (1997).
35. Nordlund, K. *et al.* Defect production in collision cascades in elemental semiconductors and fcc metals. *Phys. Rev. B* **57**, 7556–7570 (1998).
36. Ghaly, M., Nordlund, K. & Averback, R. S. Molecular dynamics investigations of surface damage produced by kiloelectronvolt self-bombardment of solids. *Philos. Mag. A* **79**, 795–820 (1999).
37. Samela, J., Kotakoski, J., Nordlund, K. & Keinonen, J. A quantitative and comparative study of sputtering yields in Au. *Nucl. Instrum. Methods Phys. Res. B* **239**, 331–346 (2005).

## Acknowledgments

S.A.N. and M.P.B. were supported by the National Science Foundation through the Division of Mathematical Sciences, M.P.B. was additionally supported through the Harvard MRSEC and the Kavli Institute for Bionano Science and Technology at Harvard University. M.J.A. and C.S.M. were supported by Department of Energy grant DE-FG02-06 ER46335. The work of J.S., L.B., M.B., D.F. and K.N. was performed within the Finnish Centre of Excellence in Computational Molecular Science (CMS),

financed by The Academy of Finland and the University of Helsinki; grants of computer time from the Center for Scientific Computing in Espoo, Finland, are gratefully acknowledged. We also thank M.J. Baldwin, N. Kalyanasundaram and H.T. Johnson for helpful discussions.

### Author contributions

S.A.N. derived the theoretical framework and generated phase diagram predictions. J.S. developed the amorphous Si simulation cells and carried out 100 and 250 eV MD simulations. S.A.N. and J.S. together developed the method of transferring the atom displacement information to the theoretical framework. L.B. carried out the 1 keV and some of the 100 eV simulations. M.B. and F.D. supervised the work of L.B. and participated in the analysis of results at 1 keV. C.S.M. performed the estimation of the viscous flow coefficient  $B$  and drafted the corresponding portion of the manuscript. K.N. developed the MD simulation code used, supervised the initial stages of the work of J.S., and made the analysis of displacements in W. M.P.B. supervised the theoretical

work of S.A.N. M.J.A. identified the problem, suggested the utility of the moments of the crater function, supervised many aspects of the work and, together with K.N., established the overall collaboration. S.A.N. drafted most of the manuscript, J.S. drafted MD-specific portions, and M.J.A. and K.N. guided revisions.

### Additional information

**Supplementary Information** accompanies this paper at <http://www.nature.com/naturecommunications>

**Competing financial interests:** The authors declare no competing financial interests.

**Reprints and permission** information is available online at <http://npg.nature.com/reprintsandpermissions/>

**How to cite this article:** Norris, S. A. *et al.* Molecular dynamics of single-particle impacts predicts phase diagrams for large scale pattern formation. *Nat. Commun.* 2:276 doi: 10.1038/ncomms1280 (2011).

## Supplementary Methods

**Simulation Methods** In molecular dynamics simulations, impact-induced structural deformations can be detected only in a well relaxed silicon structure. A stress existing within the material as a result of incomplete relaxation of the structure before the simulation can induce displacements of silicon atoms upon impact that far exceed the direct effects of impact in magnitude. For example, our test simulations showed that a structure created by annealing silicon in MD is not dense enough to model the real amorphous silicon. The surface of such a structure collapses upon impact. It is possible to relax the internal stresses by bombarding the surface with silicon atoms before the actual simulation. However, the relaxation will be not uniform. Therefore, we have used the Wooten/Winer/Weaire (WWW) method <sup>31</sup>.

The WWW method is a computer algorithm that generates realistic random network models of amorphous silicon. In this method, the structure is described with positions of  $N$  atoms and a list of bonds between the atoms. After a random switch of two bonds, the structure is relaxed using an inter-atomic potential <sup>38,39</sup>. In connection to the structural relaxation, the Berendsen pressure control algorithm is used to relax the diagonal components of the pressure tensor to zero <sup>40</sup>. The algorithm is computationally demanding and therefore it is possible to fully optimize only relatively small structures of a few thousand atoms. Therefore, the optimized block must be copied and the copies joined to create an optimized silicon structure large enough for impact simulations. Our tests showed that the best approach is to partially optimize a rather large (10x10x10 nm) building block instead of building the structure of very small fully optimized blocks. The latter approach can induce artificial internal shear stresses in spite of the optimization (note that pressure control at periodic boundaries in an orthogonal cell does not necessarily remove the non-diagonal, shear components of the stress tensor). The optimization of a 10x10x10 nm amorphous silicon structure was achieved using a parallelized implementation of the WWW algorithm.

After the WWW optimization phase, the structure and the surface were relaxed in MD using the EDIP potential, before it was used in the actual impact simulations. The structure used in the simulations was built of four identical optimized blocks. The density was 2.5 g/cm<sup>3</sup>, which indicates that the structure is dense and not likely to collapse upon

impact. Two-thirds of the silicon atoms had four neighbors, the others had five neighbors, which is also a sign of a dense structure. In a perfect amorphous network, all silicon atoms should have four neighbors. However, the test with structures built of smaller blocks that were better optimized than the 10x10x10 nm structure showed that the behavior of the moments as a function of the impact angle are very similar as those reported in the main article.

To simulate irradiation of bulk silicon samples, we have used periodic boundary conditions with slab boundary conditions (free boundary in the incoming ion direction, and periodic boundaries in the other two lateral directions). The bottom 1 nm layer of atoms in the simulation cell were held fixed, and temperature scaling was also applied to the atoms in a 1 nm thick layer above it. A border region of 1 nm thickness in the lateral directions was cooled during the simulations. The role of the cooling zones is to prevent shock waves and phonons to re-enter the impact area via the periodic boundaries. The size of the simulation box (20x20x10 nm) was chosen to be large enough to contain not only the area containing the crater but also the area of small deformations which reach 5-7 nm from the impact point.

In addition to the good amorphous silicon structure and cooling of the boundaries, the quality of the repulsive Ar-Si potential affects the outcome of impact simulations. The kinetic energy of the impacting Ar atom is deposited first in relatively strong Ar-Si collisions where the atoms come close each other. The repulsive Ar-Si potential used in this study is calculated using density-functional-theory calculations utilizing a numerical basis sets. This method is shown<sup>34</sup> to give a more accurate repulsive potential than the standard universal ZBL potential<sup>41</sup>. The same method was used to create Si-Si short-range repulsive potential which was smoothly joined to the EDIP potential. This ensures that the possible collisions between high-energy primary knock-on silicon atoms are correctly modelled.

The same initial structure was used for all simulations. However, to reduce as much as possible the effect of the initial surface structure on the measured crater statistics, the following steps were taken. First, the impact point was varied randomly over the entire surface, with (periodic) cooling regions dynamically re-assigned for each simulation so as to be maximally distant from the impact point. Second, the azimuthal angle was var-



ied randomly, and only the atoms within 7.5 nm of the impact point were included in the moment calculations (i.e., cooling zones and corners of the square box were ignored). Last, the global average – or “background” – displacement (over all simulations at a given impact angle) was subtracted from each individual displacement before analysis, as described in Supplementary Figure S1. Because we varied the impact point and azimuthal angle randomly, this global average ought to be zero for a perfect target over infinite trials; subtracting the measured average over finite trials for our imperfect target thus helps to remove target-specific effects from our measurements. With this setup, 200 simulations at each impact angle were performed, which was sufficient to isolate the background displacement, and to cancel the effect of thermal vibrations which were present in the structure after impact.

A final challenge in analyzing the data arose due to a combination of the amorphous nature of the target with the periodic boundary conditions. On an ideal, very large MD target, the effect of the impact would only be felt within a finite distance from the impact point. However, to allow the gathering of data within reasonable time, a limited box size must be used, and the periodic box described above – with cooling zones – appears to be the most physically plausible way of accomplishing this. However, a periodic box always means that one is truly simulating an infinite number of simultaneous side-by-side impacts, and with a small enough domain, these impacts can generate enough co-ordinated momentum transfer to shear the entire target, especially for an amorphous target. Indeed, within our target, the average downbeam displacement of atoms was consistently a linear function of distance from the target’s rigid floor, except near the surface, where larger displacements were concentrated. This is illustrated in Supplementary Figure S2. These displacements are extremely small, but there are many atoms so displaced, and so the resulting (artificial) contribution to the first redistributive moment is larger than that due to atoms participating directly in the collision cascade.

To combat the problem of “global shear,” we measured the average downbeam displacement within different annular slices of target parallel to the surface, using inner/outer radii of 2nm/9nm (i.e., away from both the impact and the cooling boundaries). We then fit the *bottom* half of the resulting depth-dependent profile to a line using least squares, and finally subtracted the *extrapolation to the surface* of this fit from the overall displacement field, as illustrated in Supplementary Figure S2. The results localize the displacements

to within a few nanometers of the surface, which is consistent with measured amorphous layer thicknesses of 3 nm for Si irradiated by Ar at 250 eV<sup>23</sup>. In the future, we will explore the response of a larger, hybrid target consisting of a 3 nm layer of amorphous Si atop a crystalline (but not rigid) base. However, we believe our existing measurements are within the accuracy level of the other estimates in the paper.

**Moment Capture and Fitting** Here we describe in more detail how we obtain moments, how we fit them, and how we obtain the final linearized evolution equation (4). For each simulated impact with our initially flat MD target, we define a co-ordinate system  $(x, y, z)$  centered at the impact point with  $z$  pointing normal to the surface,  $x$  pointed in the direction of the projected ion path, and  $y$  perpendicular to both  $x$  and  $z$  so as to complete a right-handed co-ordinate system. Hence, the crater function  $\Delta h(x, y; \theta)$  describes the height change associated with an impact at the origin, of an ion with incidence angle of  $\theta$  from the vertical, coming from the *negative*  $x$ -direction.

After impact, we extract the moments

$$\begin{aligned} M^{(0)}(\theta) &= \iint \Delta h(x, y) \, dx \, dy \\ M_x^{(1)}(\theta) &= \iint \Delta h(x, y) x \, dx \, dy \\ M_y^{(1)}(\theta) &= \iint \Delta h(x, y) y \, dx \, dy \end{aligned} \tag{S1}$$

using the method described in<sup>21</sup>. Here, it is important to note that the first moments  $M^{(1)}$  contain both erosive and redistributive components (because the zeroeth moment  $M^{(0)}$  describes mass loss, and because redistribution is mass-conserving,  $M^{(0)}$  has no redistributive component).

Simulation sets were performed at 5-degree increments, and the average of the resulting moments were fit to Fourier functions of the form

$$\begin{aligned} M_{x-odd} &= \sum_{n=1}^3 a_n \sin(2n\theta) \\ M_{x-even} &= \sum_{n=1}^3 b_n \cos((2n-1)\theta) \end{aligned} \tag{S2}$$

These fittings reflect the observation that all moments tend to zero at  $\theta = 90^\circ$ , and also their symmetries about  $\theta = 0$  (because a positive theta indicates an ion beam coming from the negative  $x$ -direction, moments that are odd/even in  $x$  should also be odd/even in  $\theta$ ). As seen in the main text, this method does not produce perfect fits, but the use of simple Fourier modes eliminates potential model-bias, while the restriction to a small number of terms excludes inter-angle noise from the fitted curve.

**Analysis: from Moments to Coefficients** For the general reduction of moments to (non-linear) PDE terms  $P[\mathbf{x}]$ , we refer to the framework derived in <sup>21</sup>. However, in the linear case discussed here, it is sufficient to consider the linearization of the first-order term obtained by combining Equations (1) and (3) from the main text:

$$v_{\mathbf{n}}^P(\mathbf{x}) \approx \varepsilon \nabla_S \cdot (IM^{(1)}) \quad (\text{S3})$$

(in the linearization, the zeroth- and second-moment terms do not contribute to stability). Now,  $\nabla_S$  indicates a *surface* divergence, and indeed this calculation is most naturally performed in a *local* co-ordinate system associated with the surface normal and projected beam direction. In particular, both the flux  $I(\phi)$  and the moments  $M^{(i)}(\phi)$  depend on the local incidence angle  $\phi$ , while the vector  $M^{(1)}(\phi)$  is observed to always point in the direction  $\mathbf{e}_P$  of the projected beam.

Following <sup>21</sup>, surface velocities at an arbitrary point  $\mathbf{x}$  will be calculated in a *local* co-ordinate system  $(U, V, W)$  centered at  $\mathbf{x}$ , where  $\mathbf{e}_W = \mathbf{n}$  corresponds to the surface normal,  $\mathbf{e}_U = \mathbf{e}_P$  corresponds to the *downbeam* direction associated with the projected ion beam, and  $\mathbf{e}_V = \mathbf{e}_W \times \mathbf{e}_U$ . In this system the surface is described locally by the equation  $W = H(U, V)$ , the ion flux is  $I = I_0 \cos(\phi(U, V))$ , and the (vector) first moment is  $M^{(1)} = M_X^{(1)}(\phi(U, V)) \mathbf{e}_P(U, V)$ , where  $M_X^{(1)}(\phi)$  is measured from MD. (Note that both  $\phi$  and  $\mathbf{e}_P$  depend on the slowly-varying co-ordinates  $U$  and  $V$ .) Now, as described in <sup>21</sup>, it is sufficient for the purposes of calculating one surface divergence to approximate  $H(U, V)$  via

$$H \approx \frac{1}{2} (H_{UU}U^2 + 2H_{UV}UV + H_{VV}V^2). \quad (\text{S4})$$

where  $H_{UU}$ ,  $H_{UV}$ , and  $H_{VV}$  describe the surface curvature at  $\mathbf{x}$ . All other variable quan-

tities can then be approximated *in the vicinity of*  $\mathbf{x}$  to first order in  $(U, V)$  via:

$$\begin{aligned}\mathbf{n} &\approx \left\langle -\frac{\partial H}{\partial U}, -\frac{\partial H}{\partial V}, 1 \right\rangle \\ \mathbf{e}_P &\approx \left\langle 1, -\cot(\phi_0) \frac{\partial H}{\partial V}, \frac{\partial H}{\partial U} \right\rangle, \\ \cos(\phi) &\approx \cos(\phi_0) + \frac{\partial H}{\partial U} \sin(\phi_0)\end{aligned}\tag{S5}$$

where  $\phi_0 = \phi(0, 0)$ . When we now take the surface divergence  $\nabla_S = (\partial_U, \partial_V)$  and evaluate at  $(U, V) = \mathbf{0}$  (i.e., at  $\mathbf{x}$ ), we obtain in the local co-ordinate system

$$v_{\mathbf{n}}^P(\mathbf{x}) \approx \varepsilon \nabla_S \cdot (IM^{(1)}) = \varepsilon I_0 [S_U(\phi_0) H_{UU} + S_V(\phi_0) H_{VV}]\tag{S6}$$

where

$$\begin{aligned}S_U(\phi) &= \frac{d}{d\phi} \left[ M_X^{(1)}(\phi) \cos(\phi) \right] \\ S_V(\phi) &= M_X^{(1)}(\phi) \cos(\phi) \cot(\phi)\end{aligned}\tag{S7}$$

(Note: references<sup>26, 27</sup> state a different pair of coefficients than seen in Equation (S7), without presenting the method used to obtain them. The functional dependence on  $M_X^{(1)}(\phi)$  of those coefficients result in predictions at odds with existing results in the literature for the simple model  $M_X^{(1)}(\phi) = \sin(\phi)$ ; see e.g. references<sup>16, 17, 11</sup>.)

Equation (S6) is linear in the local co-ordinates, but is in general nonlinear in the lab frame. However, for stability studies we need only the linearization of (S6) in the lab frame, which in dimensional form is simply

$$\left. \frac{\partial h}{\partial t} \right|_{\text{prompt}} = I_0 \left( S_X(\theta) \frac{\partial^2 h}{\partial x^2} + S_Y(\theta) \frac{\partial^2 h}{\partial y^2} \right)\tag{S8}$$

because, to linear order,

$$\begin{aligned}\frac{\partial^2 h}{\partial x^2} &\approx H_{UU} \\ \frac{\partial^2 h}{\partial y^2} &\approx H_{VV} \\ S_X(\phi) &\approx S_U(\phi) \\ S_Y(\phi) &\approx S_V(\phi) \\ \theta &\approx \phi_0\end{aligned}\tag{S9}$$

To expression (S8) for the prompt regime we add the linearization of the gradual regime associated with ion-enhanced viscous flow<sup>18</sup>, which is a lubrication approximation with the form

$$\left. \frac{\partial h}{\partial t} \right|_{\text{gradual}} = -B\nabla^4 h. \quad (\text{S10})$$

Adding the prompt and gradual regimes, we obtain the evolution equation (4) in the main text.

**Estimation of Viscous Flow coefficient** The materials parameter  $B$  appearing in Equation (4) of the main text is defined<sup>42</sup> as

$$B = \frac{\gamma d^3}{3\eta} \quad (\text{S11})$$

where  $\gamma$  is the surface free energy,  $d$  is the thickness of the thin amorphous layer that is being stimulated by the ion irradiation, and  $\eta$  is the layer's viscosity. We assume the surface free energy of amorphous silicon under ion irradiation to be equal to its value in the absence of irradiation; the value of  $\gamma = 1.36 \text{ J/m}^2$  measured via molecular dynamics simulations by Vauth and Mayr<sup>43</sup> happens to be numerically equal to that measured experimentally for single-crystal Si(001)<sup>44</sup>. For the amorphous layer thickness, we directly measured  $d \approx 3.0 \text{ nm}$  via cross-sectional transmission electron microscopy on samples irradiated at normal incidence and 30 degrees from normal. Finally, we estimate the viscosity of the top amorphous Si layer during irradiation to be  $\eta \approx 6.2 \times 10^8 \text{ Pa sec}$ , as shown below.

The reciprocal of viscosity is the fluidity  $\phi$ , which is generally understood to scale with the flux  $f$ , and can be expressed in the form

$$\phi = H \times N_{\text{DPAPS}} \quad (\text{S12})$$

where  $H$  is the radiation-induced fluidity, and  $N_{\text{DPAPS}}$  is the average number of displacements per atom per second. Using molecular dynamics simulations, Vauth and Mayr<sup>43</sup> report  $H = 1.04 \times 10^{-9} (\text{Pa dpa})^{-1}$  at an energy  $E = 1 \text{ keV}$  and temperature  $T = 300\text{K}$  – we use this value for our comparison with experiment, with the caveats discussed below. The average number of displacements per atom per second is given by

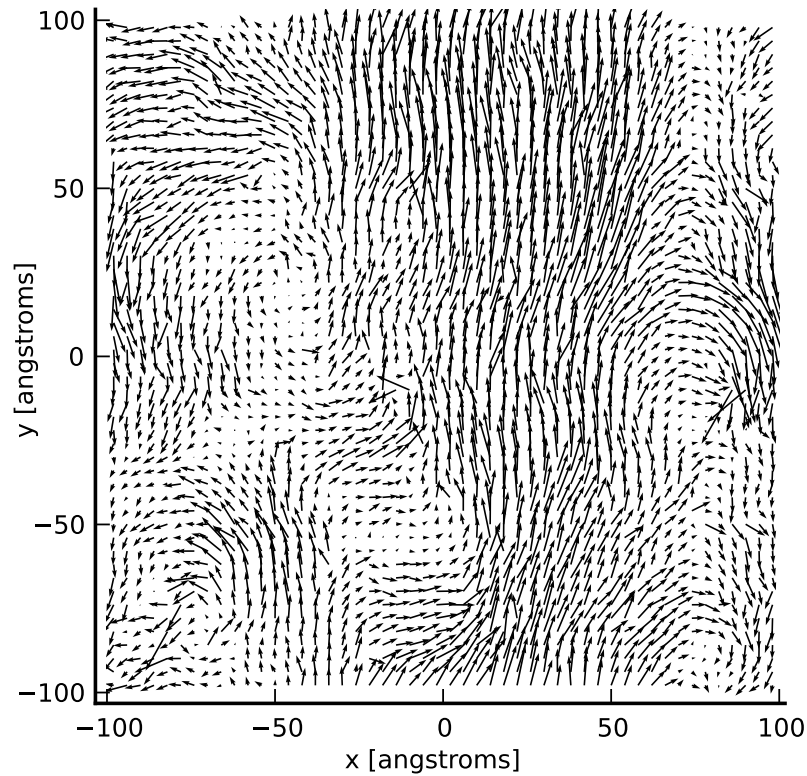
$$N_{\text{DPAPS}} = \frac{\Omega f}{d} N_{\text{recoils}}, \quad (\text{S13})$$

where  $\Omega = .02 \text{ nm}^3/\text{atom}$  is the atomic volume of silicon,  $f = 3.5 \times 10^{15} \text{ ions}/(\text{cm}^2\text{s})$  is the experimental flux in the plane perpendicular to the ion beam,  $d \approx 3 \text{ nm}$  is the amorphous layer thickness, and  $N_{\text{recoils}}$  is the number of recoils generated per ion impact. To estimate  $N_{\text{recoils}}$ , we use the Kinchin-Pease <sup>45</sup> model for the gross number of Frenkel pairs per incident ion, obtaining  $N_{\text{recoils}} = 0.8E/E_D = 6.7$ , where  $E = 250 \text{ eV}$  is the ion beam energy and  $E_D = 15 \text{ eV}$  is the displacement threshold energy of Si <sup>46</sup>. Taking all of these quantities, we obtain a value of the viscosity of

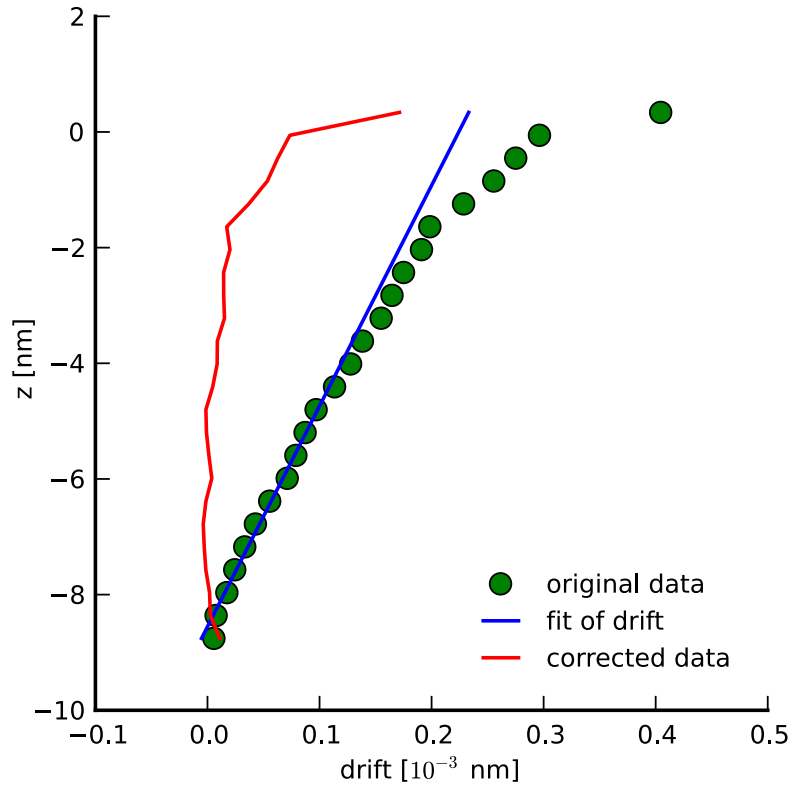
$$\eta = \frac{1}{H \times N_{\text{DPAPS}}} = 6.2 \times 10^8 \text{ Pa sec.} \quad (\text{S14})$$

As discussed above, the value for  $\eta$  listed in (S14) is associated with Vauth and Mayr's value of  $H = 1.04 \times 10^{-9} (\text{Pa dpa})^{-1}$  at an energy  $E = 1 \text{ keV}$  and temperature  $T = 300\text{K}$ . In contrast, our experiments were carried out at  $E = 250 \text{ eV}$ , and the irradiated sample is observed to reach temperatures of approximately 450 K. Hence, there is some uncertainty in our value of  $\eta$ , which translates to uncertainty regarding the vertical position of the theoretical curve in Figure 2 of the main text. For the temperature difference, Vauth and Mayr observe  $H$  to increase weakly with increasing substrate temperature, which would shift the curve upward; however, the shift would likely be less than a factor of two. As for the energy difference, in a study of CuTi, another amorphous material, Mayr et al. <sup>47</sup> found  $H$  to either increase or decrease with recoil energy depending on the details of the simulations; hence the theoretical curve in Figure 2 of the main text could shift either upward or downward for MD simulations at 250 eV, with a potential magnitude of perhaps a factor of two.

## Supplementary Figures



Supplementary Figure S1: **Removal of Background Effect from MD Target** Illustration of the background displacements observed at 60 degrees for irradiation at 250 eV. These represent displacements that survived the averaging process despite randomly varied impact positions and azimuthal irradiation directions. They are hence assumed to be due to small local stresses in the target and are removed (this assumption is strengthened by the fact that the background displacement field is very similar at all incidence angles). The arrows indicate the direction and relative magnitude of these average displacements; the largest of them are less than 0.1 angstrom.



Supplementary Figure S2: **Removal of Shearing Effect from MD Target** Illustration of the removal of shear at 60 degrees for irradiation at 250 eV. Green dots are the original layer-averaged measurement of the downbeam component of displacement, and the blue line represents a linear fit to the bottom half of the dots, extrapolated to the surface. The red line is the result of subtracting this extrapolation from the original data, which localizes the displacements to the vicinity of the surface. All data are associated with a 2nm/9nm annulus that masks the impact zone and the cooling boundary zone.



## Supplementary References

38. Mousseau, N. & Barkema, G. T. Binary continuous random networks. *J. Phys. Cond. Matt.* **16**, S5183–S5190 (2004).
39. von Alftan, S., Kuronen, A. & Kaski, K. Realistic models of amorphous silica: A comparative study of different potentials. *Phys. Rev. B* **68**, 073203 (2003).
40. Berendsen, H. J. C., Postma, J. P. M., van Gunsteren, W. F., DiNola, A. & Haak, J. R. Molecular dynamics with coupling to external bath. *J. Chem. Phys.* **81**, 3684 (1984).
41. Ziegler, J., Biersack, J. & Littmark, U. *The Stopping and Range of Ions in Matter* (Pergamon Press, New York, 1985).
42. Orchard, S. On surface levelling in viscous liquids and gels. *Appl. Sci. Res.* **11A**, 451 (1962).
43. Vauth, S. & Mayr, S. Relevance of surface viscous flow, surface diffusion, and ballistic effects in keV ion smoothing of amorphous surfaces. *Phys. Rev. B* **75**, 224107 (2007).
44. Eaglesham, D. J., White, A. E., Feldman, L. C., Moriya, N. & Jacobson, D. C. Equilibrium shape of Si. *Phys. Rev. Lett.* **70**, 1643 (1993).
45. Gnaser, H. *Low-energy ion irradiation of solid surfaces*, vol. 146 of *Springer tracts in modern physics* (Springer, 1999).
46. Wallner, G. *et al.* Defect production rates in metals by reactor neutron irradiation at 4.6 K. *J. Nucl. Mater.* **152**, 146 (1988).
47. Mayr, S. G., Ashkenazy, Y., Albe, K. & Averback, R. S. Mechanisms of radiation-induced viscous flow: Role of point defects. *Phys. Rev. Lett.* **90**, 055505 (2003).